nature photonics

ARTICLES

https://doi.org/10.1038/s41566-021-00800-3

Spontaneous pulse formation in edgeless photonic crystal resonators

Su-Peng Yu[1,2] ✉, Daniel C. Cole[1,2], Hojoong Jung[1,2], Gregory T. Moille[3,4], Kartik Srinivasan[3,4] and Scott B. Papp[1,2]

Nonlinearity in complex systems leads to pattern formation through fundamental interactions between components. With integrated photonics, precision control of nonlinearity explores novel patterns and propels applications. In particular, Kerr-nonlinear resonators support stationary states—including Turing patterns—composed of a few interfering waves, and localized solitons composed of waves across a broad spectrum. Although Turing patterns emerge from an unstable Kerr resonator with sufficiently intense excitation, Kerr solitons do not form spontaneously under constant excitation, making this useful state challenging to access. Here we explore an edgeless photonic crystal resonator (PhCR) that enables spontaneous soliton formation in place of Turing patterns. We design the PhCR nanopattern for single-azimuthal-mode engineering of a group-velocity-dispersion defect that balances Kerr-nonlinear frequency shifts in favour of the soliton state. Our experiments establish PhCR solitons as modelocked pulses through ultraprecise optical-frequency measurements. We show that nanophotonics expand the palette for nonlinear engineering, enabling new phenomena and light sources.

Integrated nonlinear photonics is a versatile engine to generate and control electromagnetic radiation, opening new application directions and enabling fundamental studies. Second- and higher-order nonlinear susceptibilities now form the basis of many photonics technologies; a good example is harmonic-[1] or difference-frequency[2] generation, which realizes laser sources from the ultraviolet to the infrared. In particular, third-order Kerr processes are ubiquitous in photonics due to intensity dependence of the refractive index, $n = n_0 + n_2 I$, where n_0 and n_2 are the linear and nonlinear indices and I is intensity. They enable spontaneous formation of stationary configurations of electromagnetic fields that effect conversion of a laser from one colour to another. More generally, modulation instability that arises from nonlinearity governs interesting behaviours in systems, ranging from quantum matter[3] to desert sand dunes[4].

Kerr resonators—optical cavities built from an n_2 material—are attractive systems for fundamental studies and applications. We understand the formation of some patterns and pulse states from the Lugiato–Lefever equation (LLE) describing the intraresonator field. A few states stand out among the diverse solution space of the LLE[5,6]: the constant-amplitude flat state energized by a sufficiently weak pump laser; the Turing pattern that emerges when the flat state is unstable; and the dissipative Kerr soliton (DKS) that is a localized pulse coexisting with—but not emerging spontaneously from—the flat state. Microresonator soliton frequency combs[7] have been engineered to support a wide range of applications, including optical communication[8,9], spectroscopy[10] and ranging[11]. Group-velocity dispersion (hereafter GVD or dispersion) engineering via the cross-sectional waveguide dimensions offers powerful control of soliton properties[12] and to suppress undesired high-order modes[13]. Moreover, exotic photonic states have been reported using unconventional resonator mode engineering[14,15].

Here we explore rebalancing the LLE to cause Kerr soliton formation from break-up of the flat state, replacing the Turing pattern. We design and fabricate edgeless photonic crystal resonators (PhCR) to accomplish this outcome, which are Kerr microresonators with their inner wall modified by an azimuthally uniform, nanopatterned shape oscillation. The ring geometry imposes the edgeless boundary condition on the photonic waveguide, opening the PhCR bandgap—thus controllably shifting the frequency—for one azimuthal mode. This point-defect in the resonance frequencies is a generalization of optical dispersion beyond the conventional polynomial orders. We program the shift to directly phase-match the soliton with the pump laser nearly on-resonance of the pump mode. Moreover, this shifts the Turing pattern off-resonance, precluding its formation. We have realized and explored spontaneous soliton formation in wide-ranging experiments, including observing the immediate transition from the flat state to the soliton, soliton pulse bandwidth control by dispersion engineering through the bulk ring dimensions, and ultraprecise measurements of the soliton repetition frequency.

Our work draws on advances in nanophotonics and photonic crystal (PhC) devices that provide access to otherwise challenging or impossible to achieve phenomena; for example, the exotic refractive phenomenon[16], strong light–matter interactions[17] and coupling to radiofrequency or phonon modes [18]. Moreover, photonic structures have been demonstrated to suppress[19] and enhance[20] nonlinear effects, engineer small mode volumes[21], create sophisticated GVD profiles[22,23], realize slow-light effects[24] and control resonator mode splittings[25]. Photonic crystal devices are dielectric structures with subwavelength spatial periodicity[26] that restrict scattering to discrete momentum values $k_m = k_0 + \frac{2m\pi}{\Lambda}$ not interacting with free-space modes, where Λ is the periodicity and m is an integer. In a photonic resonator, the bandgap imposes reflective boundaries to confine light as in a Fabry–Perot cavity[12]. In our experiments we instead use the bandgap in an edgeless boundary condition—a complete ring without edges—to modify a select mode of the PhCR. This condition, combined with an even number of nanopattern periods, frequency-aligns the bandgap to a mode of the PhCR[27].

---

[1]Time and Frequency Division, NIST, Boulder, CO, USA. [2]Department of Physics, University of Colorado, Boulder, CO, USA. [3]Microsystems and Nanotechnology Division, NIST, Gaithersburg, MD, USA. [4]Joint Quantum Institute, NIST, University of Maryland, College Park, MD, USA.
✉e-mail: supeng.yu@colorado.edu

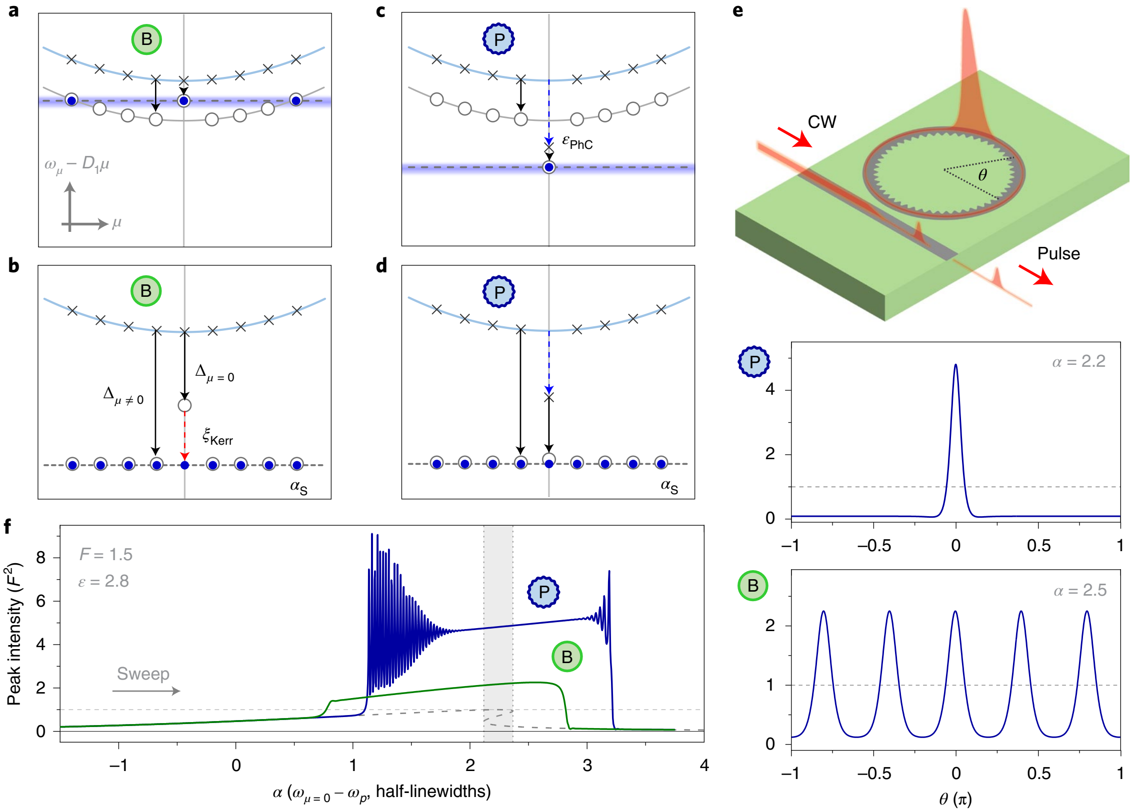

Fig. 1 | Mode structure for the Kerr resonator. Cold- and hot-cavity resonances are marked by crosses and open circles, respectively, the pump lasers are marked by dashed lines and the lights in each mode are indicated by filled circles; $\alpha_{\rm S}$ is the detuning of the DKS from the zero of the base ring dispersion curve. **a**,**b**, The Turing pattern (**a**) and DKS state (**b**) in the ring resonator (green circles) are shown along with $\xi_{\rm Kerr}$ (red dashed arrow). **c**,**d**, The PhCR resonator (blue circles) is shown with photonic crystal shifts (dashed blue arrows) at the corresponding Kerr shifts, with **c** in the flat amplitude state and **d** in the pulse state. **e**, An illustration of optical pulse formation in a photonic ring resonator. **f**, Simulated peak pulse power versus pump laser detuning for the ring and PhCR resonators, the corresponding intensity profiles are shown to the right. The sweep rate is 8.8×10^{-3} half-widths per photon lifetime. The analytic flat amplitude (dashed grey curve) shows the intensities returning to the background for both cases without the comb states. The bistability range (shaded grey area) is shown for reference.

Results

Spontaneous formation of patterns from break-up of the flat state is a critical outcome in the LLE, $\partial_\tau\psi = -(1+i\alpha)\psi - \frac{i}{2}\beta\partial_\theta^2\psi + i|\psi|^2\psi + F$, where τ is time, θ is the resonator angular coordinate in the co-moving frame, i is the imaginary unit, ψ is the intraresonator field, $-\frac{i}{2}\beta\partial_\theta^2\psi$ is the dispersion, $|\psi|^2\psi$ is the nonlinearity, F is a travelling-wave pump laser field that originates outside of the resonator with a frequency lower than the resonator mode by α (see ref. [5] for further details). We study the LLE in the Fourier basis. A pattern forms spontaneously by four-wave mixing (FWM)[5,28], constrained by a balance of the Kerr frequency shift Δ_μ of the comb mode number μ and the phase-mismatch from dispersion, $\frac{1}{2}\beta\mu^2$. We count the comb modes and the resonator modes with respect to the mode closest to the pump laser (hereafter the pump mode, $\mu=0$). Importantly, Δ_μ for each mode depends on the intraresonator field according to $\Delta_\mu = g(2N-|a_\mu|^2)$[28], where a_μ is the Fourier decomposition amplitude for μ, g the per-photon Kerr shift and N the total photon number. The term $g=1$ is a standard normalization of the LLE. Beginning with the flat state, all $a_{\mu'\neq0}=0$ and $\Delta_{\mu=0} = 2N - N = \frac{1}{2}\Delta_{\mu'\neq0}$, where the modes μ' are not pumped. The difference between self- and cross-phase modulation results in a reduced Kerr shift for the pump mode by a factor of two compared with other modes. This reduced Kerr shift enables FWM for the Turing pattern at modes $\pm\mu'$, characterized by $\frac{1}{2}\beta|\mu'|^2 - \Delta_{\pm\mu'} = -\Delta_{\mu=0}$. Conversely, the soliton is a collective state with many μ' that reach phase matching only at large α where the flat-state amplitude is insufficient to support spontaneous FWM processes. These phase-matching conditions result in the disparate generation behaviours of Turing patterns and solitons. We engineer the resonator mode frequency structure to modify the phase-matching condition, therefore controlling which state can form.

Figure 1 introduces the mode frequency structure of a ring resonator and a PhCR, emphasizing how modifying the pump mode affects Turing-pattern and Kerr-soliton generation. Figure 1a–d plots the modal detuning $\omega_\mu-(\omega_0+D_1\mu)$ for each μ (where ω_μ is the angular frequency and D_1 is the free-spectral range), showing the cold-resonator modes that correspond to each μ (crosses) and hot resonator modes (open circles). The cold resonances follow the integrated dispersion, $D_{\rm int} = \omega_\mu - \omega_0 - D_1\mu = 1/2\ D_2\ \mu^2 + \epsilon_{\rm PhC}\ (1-\delta(\mu))$, where $\epsilon_{\rm PhC}$ is the frequency shift of the pump mode and $\delta(\mu)$ is the Kronecker delta function. We further shift the hot resonances by the Kerr shift Δ_μ, indicating phase accumulation from the Kerr effect. At the onset of flat-state break-up, $\Delta_{\mu=0}$ is half that for all other modes. A natural phase matching therefore exists for FWM to μ', where the horizontal dashed line matches the shifted $D_{\rm int}$ curve (Fig. 1a). Hence the Turing pattern emerges, initially composed of pump and $\pm\mu'$ modes (blue dots). The stationary soliton state (Fig. 1b) of the ring resonator involves Kerr frequency shifts to balance dispersion across many equidistant comb modes (blue dots). The horizontal line in Fig. 1b indicates the pump laser; however, as the pump mode Kerr shift is

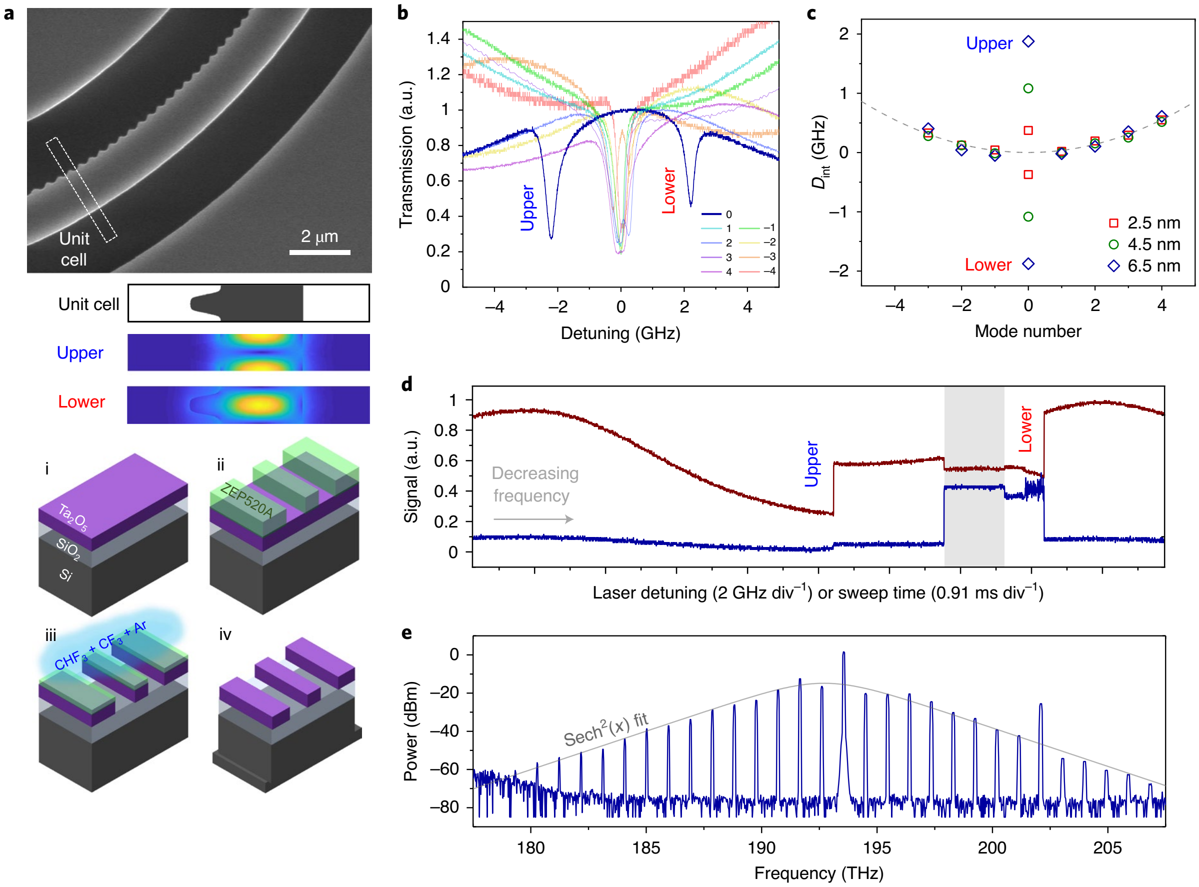

Fig. 2 | Experimental evidence for spontaneous soliton formation. **a**, An electron microscope image of the PhCR, showing the unit cell geometry and electric field profiles. Fabrication steps are shown below as (i) substrate, (ii) electron-beam lithography, (iii) reactive ion etching and (iv) dicing. Scale bar, 2 µm. **b**, Laser frequency sweep traces of the shifted mode and nearby modes. **c** Mode frequencies for resonators with varying A_{PhC}, where μ is counted relatively to the 163rd resonance mode of the ring. **d**, Laser frequency sweep traces of pump transmission (red) and comb power (blue) demonstrating a spontaneous step, where the stable pulse state is shaded in grey. **e**, Optical spectrum of the stable state.

reduced, only large α balances the Kerr mismatch $\xi_{\mathrm{Kerr}}=\Delta_{\mu\neq0}-\Delta_{\mu=0}$. This detuning precludes spontaneous formation of the Turing pattern, but also the formation of solitons, as the flat state amplitude is too low to break into patterns[5] (see Supplementary Section 2 for detailed calculations of ξ_{Kerr}).

With a PhCR, we program the frequency shift ϵ_{PhC} to alleviate the ξ_{Kerr} of the soliton state. The negative shift of both the cold and hot resonator at comb mode μ are apparent in Fig. 1c,d. Under this condition, the Turing pattern no longer emerges from the flat state when the pump mode is energized, as the natural FWM phase matching is removed (see the horizontal line in Fig. 1c). Importantly, ϵ_{PhC} shifts the cold pump mode towards a lower frequency by an amount commensurate with ξ_{Kerr}, thereby compensating for the reduced Kerr shift on the pump mode, bringing it approximately onto resonance with the pump laser. Without the Turing pattern as a competing state, the flat amplitude deterministically breaks up into the soliton state, the unique stable state for the PhCR. In summary, the high flat amplitude on resonance must break into patterns[5], the soliton state is one pattern it could create due to phase matching by the PhCR, and it is the only state available as the Turing patterns are eliminated; thus, the flat amplitude deterministically breaks into the soliton state. Operationally, soliton formation in a PhCR proceeds with the configuration shown in Fig. 1e. We integrate a PhCR device and a coupling waveguide with a silicon chip. The frequency shift ϵ_{PhC} is controlled by the nanopatterning on the ring, whereas the pump laser field F couples evanescently into the PhCR from a waveguide. The continuous-wave pump laser energizes the PhCR and creates a stable soliton pulse-train at the output.

We use the LLE to calculate ψ during a sweep of the pump laser frequency across the pump mode to verify the physical understanding presented above (see Supplementary Section 1 for an LLE with the mode shift). Figure 1e shows the peak intensity $|\psi|^2$ versus detuning for the ordinary ring resonators and PhCRs. All frequency variables including α and ϵ_{PhC} are in unit of half-width-half-max linewidths unless otherwise specified, and all intensities are shown in units of F^2, the resonant flat amplitude intensity. Aside from changing ϵ_{PhC} from 0 to 2.8 to activate the PhCR frequency shift, both simulations are performed with the same conditions, namely $F=1.5$, $\beta=-0.17$. The ring resonator produces the five-lobe Turing pattern (lower panel) as the pump detuning is swept completely across resonance, corresponding to a range of α from −2 to 4. We then introduce the PhCR case and carry out the same α sweep. In contrast to the ring resonator case, a single pulse forms with abrupt onset. Neither Turing patterns nor chaotic states form during the sweep. Furthermore, the pulse demonstrates two distinct sections of oscillatory stages, known as breather soliton states[7]. The curious reappearance of the breather state at the end of the sweep also contrasts with ring resonator soliton behaviour, and we observe this in our experiments.

Figure 2 presents our PhCR devices and experimental evidence for spontaneous soliton formation, according to the principles laid out above. We create a PhCR device with the oscillatory nanopattern

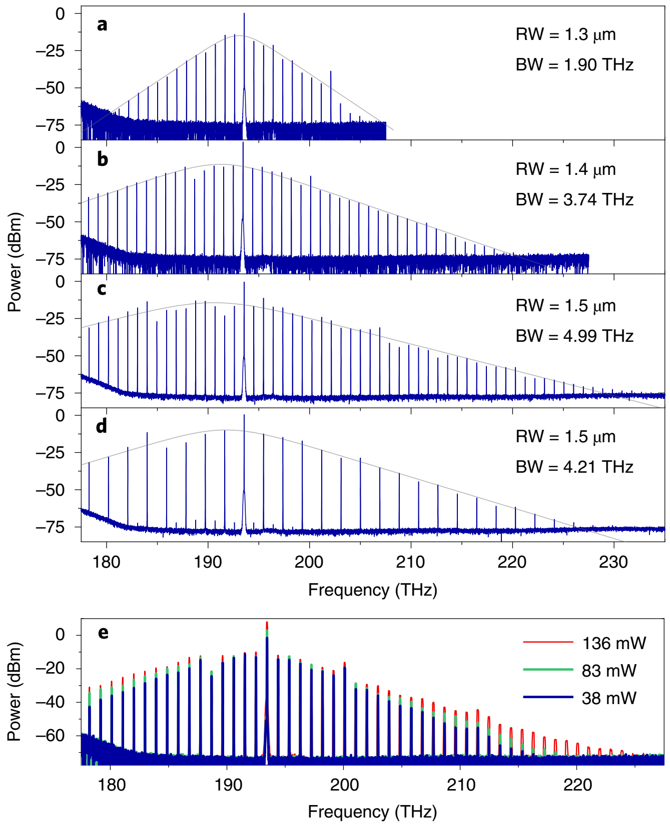

Fig. 3 | Optical spectra from PhCRs. a–c, Optical spectra from PhCRs with average ring width 1.3 µm (**a**), 1.4 µm (**b**) and 1.5 µm (**c**). **d**, The two-pulse state on the 1.5 µm device. The grey traces are fits with the form $y = A_0 + 10\log(\text{sech}^2((x - x_0)/\text{BW}))$, where the BW parameter characterizes the bandwidth. **e**, Spectra versus power for the RW = 1.4 µm device.

indicated in Fig. 2a. A unit cell of the pattern is defined by a sinusoidal shape, characterized by the pattern periodicity and peak-to-peak amplitude $A_{\rm PhC}$. The periodicity enforces a photonic bandgap that necessarily overlaps one particular PhCR mode (denoted as the pump mode $\mu = 0$) in the 1,550 nm wavelength range, owing to an equal azimuthal mode number of pattern periods and optical-mode fringes. The bandgap lifts the degeneracy of counter-propagating light in the PhCR, creating modes that are shifted to higher and lower frequencies by $\epsilon_{\rm PhC}$. As the nanopattern is edgeless (that is, circumferentially uniform), high resonator Q is maintained. The properties of the other PhCR modes ($\mu \neq 0$) with $\epsilon_{\rm PhC} \approx 0$ (including nonlinearity and GVD) are preserved under the geometric modification. In particular, the GVD depends sensitively on the thickness and ring-waveguide width (RW) as in a ring resonator. We fabricate our devices from a 570-nm-thick tantalum pentoxide (Ta_2O_5, hereafter tantala) photonics layer[29], which is deposited on an oxidized silicon wafer. We use electron-beam lithography to define the photonics pattern for a wafer, and we transfer it to the tantala layer by use of fluorine reactive ion etching. A final ultraviolet lithography process defines several chips on the wafer, and we dry-etch facets in the tantala and oxide layers, and the silicon wafer (see Methods for more details). In our experiments with PhCRs, we characterize $\epsilon_{\rm PhC}$ by spectroscopy measurements. We fabricate up to ~75 PhCRs on a chip with a systematic variation of $\epsilon_{\rm PhC}$ (few linewidths) and the waveguide-resonator coupling gap (~200 nm) to optimize the conditions for spontaneous soliton formation. We couple light to and from the chip with a standard lensed-fibre system to measure $\epsilon_{\rm PhC}$. Using a 1,550-nm tunable laser as input, we record the transmission at the output with a photodetector. Figure 2b shows several PhCR mode resonances in the 1,550-nm band (with applied frequency offsets so the resonances coincide) that demonstrate a single mode frequency splitting. We label the non-degenerate modes as upper and lower, with the latter at a setting of $\epsilon_{\rm PhC}$ consistent with spontaneous soliton formation. Our experiments focus on gaps for near-critical coupling, and these data indicate a loaded PhCR Q of ~400,000. By adjusting the nanopattern amplitude through electron-beam lithography, we systematically vary $\epsilon_{\rm PhC}$ (see Fig. 2c). In the range of $A_{\rm PhC}$ used in this work, the Q factors are unaffected, compared with ring resonators fabricated on the same wafer, but the ultimate Q reachable by the PhCR has yet to be explored. With a nanopattern amplitude of only a few nanometres, we control $\epsilon_{\rm PhC}$ for the $\mu = 0$ mode, whereas the $\mu' \neq 0$ modes exhibit an anomalous GVD of $D_2 = 2\pi \cdot 69.0\,\text{MHz}$ per mode. The results confirm our fabrication process provides the high device geometry resolution and low optical loss to build PhCRs to support the pulses.

We search for spontaneous soliton formation in a PhCR with $\epsilon_{\rm PhC} = 2.2$ by sweeping the frequency of the pump laser with ~36 mW of on-chip power; Fig. 2d presents a ~20 GHz sweep range from high to low frequencies that span the upper and lower resonances. We use photodetectors to monitor transmission through the PhCR device (red trace) and the power of generated comb modes (blue trace), which we obtain by filtering out the pump. These data show the presence of thermal bistability effects—which distort the resonances into a triangle shape—and the effects of nonlinear comb generation. In particular, we observe no comb power at the upper resonance, as the upper mode is shifted away from the μ' modes needed for FWM. Whereas at the lower resonance we observe immediate comb formation, corresponding to the step change in comb power in agreement with our simulation in Fig. 1f. We assess that this nonlinear state on the lower resonance (indicated by the shaded area in Fig. 2d) is a DKS that spontaneously forms under certain conditions of pump power and laser detuning. We also observe a nonlinear state on the lower resonance that exhibits relatively higher comb power variance, which is probably a breather state as indicated theoretically in Fig. 1f. The breather state at higher detuning than the stable state suggests a modified optical state phase diagram yet to be explored. Operationally, we adjust the pump power to maximize the pump frequency existence range of the low-noise spontaneous soliton step, and we hand adjust the laser frequency into this range. It is under these conditions that we record the optical spectrum (Fig. 2e) of the soliton comb, which exhibits a clear $\text{sech}^2(x)$ profile as shown by the grey line. So far we have observed spontaneous solitons in $\epsilon_{\rm PhC} = 2$–7 half-widths; we present measurements of such spontaneous solitons in the remainder of this work.

We attribute the ease of spontaneous soliton capture to desirable thermal behaviours of the PhCR. Conventionally, in a ring resonator device, capturing and sustaining a soliton is difficult as a result of rapid heating and cooling of the microresonator[30,31]. Soliton initiation in the ring resonator under continuous-wave excitation is preceded by Turing patterns or chaotic states, which are multiple-pulse states with high average intensity. Conversely, the desired soliton state is a single pulse with a relatively low average intensity. The root of thermal instability is hence the transition of a nonlinear state in a microresonator. The spontaneous solitons of the PhCR resonator offer two primary advantages: first, in soliton initiation, we bypass the high average intensity states and avoid their heating effects to the resonator; second, we keep the pump laser on-resonance in the soliton state (note the drop in transmission trace in Fig. 2d as the pulse forms, indicating a more resonant condition), therefore minimizing changes to the in-resonator pump amplitude as the soliton forms. Together, these factors minimize the intensity changes in the PhCR, allowing pulses capturing by hand-tuning alone.

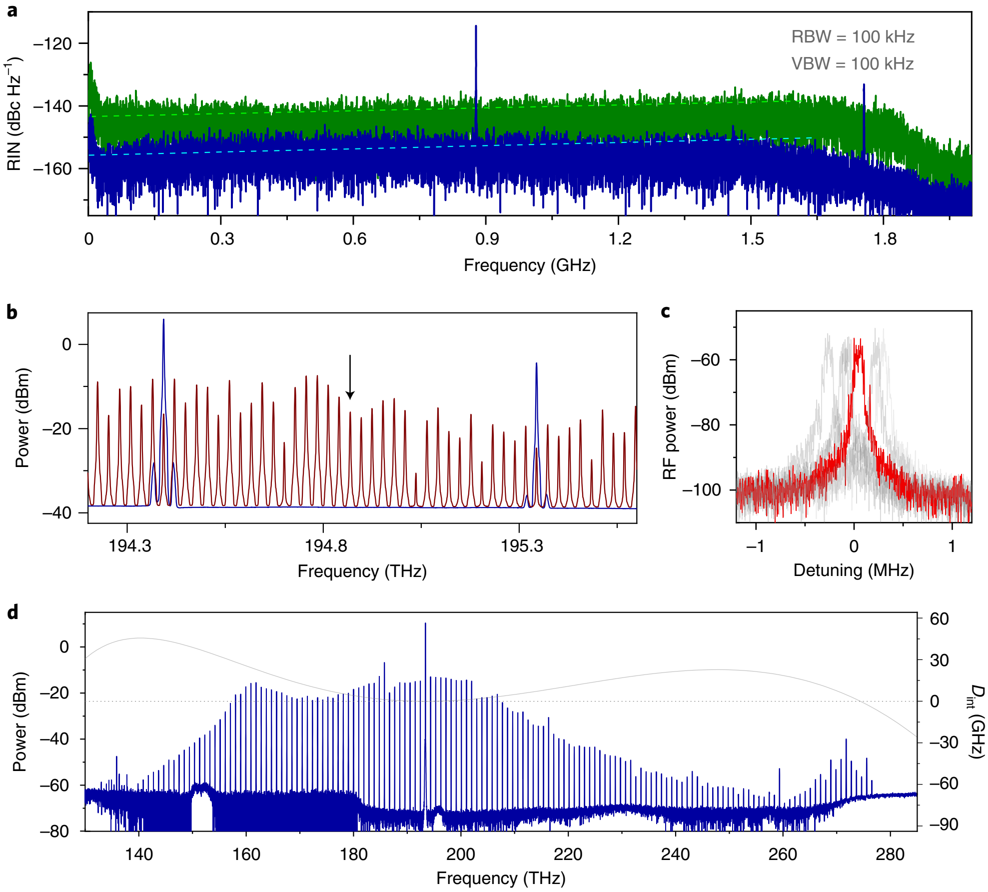

Fig. 4 | Intensity and frequency noise measurements. **a**, The relative intensity noise on the comb power of a breather (blue) and quiet (green) states measured with resolution and video bandwidths (RBW, VBW) at 100 kHz. The dashed lines show the detector noise floor corresponding to the carrier power. **b**, Bridging between the 1 THz separation between comb lines (blue) by creating sidebands (red) using electro-optic modulation. The arrow indicates the overlapping mode. **c**, Electronic beatnote from the overlapping mode. The grey traces show five consecutive measurements. **d**, An optical spectrum of a broadband soliton. The calculated integrated dispersion is shown in grey. The dotted horizontal line indicates $D_{\mathrm{int}}=0$.

To explore the universality of spontaneous soliton formation, we demonstrate soliton bandwidth control by tuning the GVD of the PhCR and the pump laser power. We control the GVD directly by varying the RW from 1.3 to 1.5 μm, providing decreasing anomalous GVD that we can understand from finite-element calculation of the PhCR resonator mode structure. Based on the LLE, this change should affect an increasing soliton bandwidth. We tune into the soliton states on these devices by hand and acquire their optical spectra (Fig. 3a–c). The spectrum bandwidth broadens with decreasing anomalous GVD as expected. Interestingly, we acquired a stable two-pulse state at lower detuning on the $\mathrm{RW}=1.5\,\mu\mathrm{m}$ device (shown in Fig. 3d). The two-pulse state suggests that the parameter space of the PhCR—an interplay between dispersion and mode shift—supports more steady states beyond the single spontaneous pulse. We also varied the pump laser power for the $\mathrm{RW}=1.4\,\mu\mathrm{m}$ device (see Fig. 3e), resulting in widening of the spectral envelope consistent with the DKS; however, unlike the conventional case in which increasing pump power monotonically lengthens the soliton existence range[32], the PhCR produces strong breather states at high power. More studies are underway to fully explore this behaviour. In this work, a typical ~75-device chip would yield ~10 devices in the correct parameter range, within which approximately half of the tested devices create the spontaneous pulses. The limit being some devices demonstrate high thermal shift rate for the upper mode, causing the lower mode to become obstructed. Ongoing work optimizing the annealing and processing of the tantala material is expected to reduce optical absorption and alleviate the thermal issue.

Stationary microresonator solitons output an optical pulse-train with a fixed period, which comprises a low-noise, equidistant frequency comb suitable for optical–frequency measurements[33,34]. Verifying the spectral-noise properties of spontaneous solitons in PhCRs is therefore of utmost importance. Figure 4 presents intensity and frequency noise measurements (excluding the pump laser) of a spontaneous soliton, which we generate in a device with $\mathrm{RW}=1.4\,\mu\mathrm{m}$, $\epsilon_{\mathrm{PhC}}=3.0$. The relative intensity noise (Fig. 4a) of a stationary soliton and a breather soliton is below $-140\,\mathrm{dBc\,Hz^{-1}}$ over a Fourier frequency range to 1.8 GHz. Here the photodetected soliton power is 282 μW and the spur-free dynamic range is excellent, whereas the breather state manifests a single peak at 878 MHz and supports higher power and hence lower relative intensity noise. These measurements are currently limited by the comb power and the detector noise floor.

To measure the ~1 THz PhCR soliton repetition frequency, we apply electro-optic phase modulation to create a low-frequency heterodyne beat between two soliton comb modes[34]. We choose an electro-optic drive frequency such that the ±17th-order sidebands (arrow in Fig. 4b) generate an optical heterodyne on a photodetector after filtering out that pair. We identify the tone thus generated as the heterodyne, as it varies with the electro-optic drive frequency at 34.2 MHz/MHz in agreement with the sideband orders. We present the heterodyne spectrum in Fig. 4c, which shows the typical lineshape with ~50 kHz linewidth and <1 MHz fluctuations. The thermal drift rate at ~100 kHz s^{-1} over the 1 THz repetition rate corresponds to an Allan deviation on the order of 10^{-7} at 1 s. We attribute these properties to the thermal noise[35] and thermal drift of the microresonator under free-running conditions. The timescales for such noise can be countered by feedback loops, for example, using the stabilized laser and the f–2f self-referencing methods[34]. The PhCR comb tunes at commensurate rate as the conventional DKS devices both thermally and in response to pump laser detuning. With this in mind, we demonstrate a PhCR device with optimized dispersion to create a spontaneous DKS with near-octave bandwidth (Fig. 4d). The F^2 value for this trace is estimated to be 8.7, normalized to threshold power of $\mu = \pm 1$ modes. We observe a dispersive wave at 273 THz, while the long-wave cut-off at 140 THz is a result of the air-clad bus waveguide losing guiding. We anticipate these optimized devices to enable f–2f self-referencing in the future.

In conclusion, we have presented spontaneous and deterministic generation of Kerr solitons in edgeless PhCRs, enabled by compensating $\xi_{\rm Kerr}$ between the pulse state and its pump mode. Mode shifting by nanopatterning enables spontaneous generation, whereas we retain the capability to engineer broadband dispersion with the bulk ring geometry. The importance of the nanophotonic capabilities presented in this work is twofold: first, the ability to controllably shift modes while maintaining the bulk dispersion profile provides a tool to explore the physics occurring in a nonlinear process. Here the capability modifies the behaviour of the pump mode, but we envision applications such as direct engineering of dispersive waves[36] or soliton crystals[37], potentially enabling inverse design methods for arbitrary desired waveforms. Second, the spontaneous formation nature of pulses demonstrated here considerably reduces the system complexity for a soliton formation and stabilization system, enabling low power consumption, packaging-friendly devices or integrated systems with multiple independent pulse sources. Future development towards a unified system with injection-locked devices[38] using the controlled back-scattering of the PhCR and on-chip nonlinear isolators[39] integrated to the same photonic platform as the PhCR, will facilitate laser integration. We envision that the spontaneous pulse devices such as the PhCRs presented in this work will become building blocks for future nonlinear optics and integrated photonics technologies.

Online content

Any methods, additional references, Nature Research reporting summaries, source data, extended data, supplementary information, acknowledgements, peer review information; details of author contributions and competing interests; and statements of data and code availability are available at https://doi.org/10.1038/s41566-021-00800-3.

Received: 1 May 2020; Accepted: 18 March 2021;
Published online: 29 April 2021

References

1. Hickstein, D. D. et al. High-harmonic generation in periodically poled waveguides. *Optica* **4**, 1538–1544 (2017).
2. Tadanagaa, O. et al. Efficient 3-m difference frequency generation using direct-bonded quasi-phase-matched LiNbO$_3$ ridge waveguides. *Appl. Phys. Lett.* **88**, 061101 (2006).
3. Carr, L. D. & Brand, J. Spontaneous soliton formation and modulational instability in Bose–Einstein condensates. *Phys. Rev. Lett.* **92**, 040401 (2004).
4. Parteli, E. J. R., Andrade, J. S. Jr & Herrmann, H. J. Transverse instability of dunes. *Phys. Rev. Lett.* **107**, 188001 (2011).
5. Godey, C., Balakireva, I. V., Coillet, A. & Chembo, Y. K. Stability analysis of the spatiotemporal Lugiato–Lefever model for Kerr optical frequency combs in the anomalous and normal dispersion regimes. *Phys. Rev. A* **89**, 063814 (2014).
6. Qi, Z. et al. Dissipative cnoidal waves (turing rolls) and the soliton limit in microring resonators. *Optica* **6**, 1220–1232 (2019).
7. Kippenberg, T. J., Gaeta, A. L., Lipson, M. & Gorodetsky, M. L. Dissipative Kerr solitons in optical microresonators. *Science* **361**, eaan8083 (2018).
8. Marin-Palomo, P. et al. Microresonator-based solitons for massively parallel coherent optical communications. *Nature* **546**, 274–279 (2017).
9. Fülöp, A. et al. High-order coherent communications using mode-locked dark-pulse Kerr combs from microresonators. *Nat. Commun.* **9**, 1598 (2018).
10. Suh, M.-G., Yang, Q.-F., Yang, K. Y., Yi, X. & Vahala, K. J. Microresonator soliton dual-comb spectroscopy. *Science* **354**, 600–603 (2016).
11. Trocha, P. et al. Ultrafast optical ranging using microresonator soliton frequency combs. *Science* **359**, 887–891 (2018).
12. Yu, S.-P. et al. Tuning Kerr-soliton frequency combs to atomic resonances. *Phys. Rev. Appl.* **11**, 044017 (2019).
13. Kordts, A., Pfeiffer, M. H. P., Guo, H., Brasch, V. & Kippenberg, T. J. Higher order mode suppression in high-Q anomalous dispersion sin microresonators for temporal dissipative Kerr soliton formation. *Opt. Lett.* **41**, 452–455 (2016).
14. Lobanov, V., Lihachev, G., Kippenberg, T. J. & Gorodetsky, M. Frequency combs and platicons in optical microresonators with normal GVD. *Opt. Exp.* **23**, 7713–7721 (2015).
15. Xue, X. et al. Mode-locked dark pulse Kerr combs in normal-dispersion microresonators. *Nat. Photon.* **9**, 594–600 (2015).
16. Kocaman, S. et al. Zero phase delay in negative-refractive-index photonic crystal superlattices. *Nat. Photon.* **5**, 499–505 (2011).
17. Miura, R. et al. Ultralow mode-volume photonic crystal nanobeam cavities for high-efficiency coupling to individual carbon nanotube emitters. *Nat. Commun.* **5**, 5580 (2014).
18. Fang, K., Matheny, M. H., Luan, X. & Painter, O. Optical transduction and routing of microwave phonons in cavity-optomechanical circuits. *Nat. Photon.* **10**, 489–496 (2016).
19. Petrovich, M. N., Poletti, F., van Brakel, A. & Richardson, D. J. Robustly single mode hollow core photonic bandgap fiber. *Opt. Exp.* **16**, 6 (2008).
20. Sharma, M., Konar, S. & Khan, K. R. Supercontinuum generation in highly nonlinear hexagonal photonic crystal fiber at very low power. *J. Nanophoton.* **9**, 093073 (2015).
21. Hu, S. & Weiss, S. M. Design of photonic crystal cavities for extreme light concentration. *ACS Photon.* **3**, 1647–1653 (2016).
22. Kim, S. et al. Dispersion engineering and frequency comb generation in thin silicon nitride concentric microresonators. *Nat. Commun.* **8**, 372 (2017).
23. Moille, G., Li, Q., Kim, S., Westly, D. & Srinivasan, K. Phased-locked two-color single soliton microcombs in dispersion-engineered Si$_3$N$_4$ resonators. *Opt. Lett.* **43**, 2772–2775 (2018).
24. McGarvey-Lechable, K. et al. Slow light in mass-produced, dispersion-engineered photonic crystal ring resonators. *Opt. Exp.* **25**, 3916–3926 (2017).
25. Lu, X., Rogers, S., Jiang, W. C. & Lin, Q. Selective engineering of cavity resonance for frequency matching in optical parametric processes. *Appl. Phys. Lett.* **105**, 151104 (2014).
26. Joannopoulos, J., Villeneuve, P. R. & Fan, S. Photonic crystals: putting a new twist on light. *Nature* **386**, 143–149 (1997).
27. McGarvey-Lechable, K. & Bianucci, P. Maximizing slow-light enhancement in one-dimensional photonic crystal ring resonators. *Opt. Exp.* **22**, 26032–26041 (2014).
28. Herr, T., Gorodetsky, M. L. & Kippenberg, T. J. Dissipative Kerr solitons in optical microresonators. In *Nonlinear Optical Cavity Dynamics: From Microresonators to Fiber Lasers* Ch. 6 (Wiley-VCH Verlag GmbH, 2015).
29. Jung, H. et al. Kerr solitons with tantala ring resonators. In *Proceedings to Nonlinear Optics Conference—OSA Technical Digest* NW2A.3 (The Optical Society, 2019).
30. Stone, J. R. et al. Thermal and nonlinear dissipative-soliton dynamics in Kerr-microresonator frequency combs. *Phys. Rev. Lett.* **24**, 063902 (2018).
31. Brasch, V., Geiselmann, M., Pfeiffer, M. H. P. & Kippenberg, T. J. Bringing short-lived dissipative Kerr soliton states in microresonators into a steady state. *Opt. Exp.* **24**, 29312–29320 (2016).
32. Guo, H. et al. Universal dynamics and deterministic switching of dissipative Kerr solitons in optical microresonators. *Nat. Phys.* **13**, 94–102 (2017).
33. Briles, T. C. et al. Interlocking Kerr-microresonator frequency combs for microwave to optical synthesis. *Opt. Lett.* **43**, 2933–2936 (2018).
34. Drake, T. E. et al. Terahertz-rate Kerr-microresonator optical clockwork. *Phys. Rev. X* **9**, 031023 (2019).
35. Drake, T. E., Stone, J. R., Briles, T. C. & Papp, S. B. Thermal decoherence and laser cooling of Kerr microresonator solitons. *Nat. Photon.* **14**, 480–485 (2020).

36. Matsko, A. B., Liang, W., Savchenkov, A. A., Eliyahu, D. & Maleki, L. Optical Cherenkov radiation in overmoded microresonators. *Opt. Lett.* **41**, 2907–2910 (2016).
37. Cole, D. C., Lamb, E. S., Del'Haye, P., Diddams, S. A. & Papp, S. B. Soliton crystals in Kerr resonators. *Nat. Photon.* **11**, 671–676 (2017).
38. Shen, B. et al. Integrated turnkey soliton microcombs. *Nature* **582**, 365–369 (2020).
39. Bino, L. D. et al. Microresonator isolators and circulators based on the intrinsic nonreciprocity of the Kerr effect. *Optica* **5**, 279–282 (2018).

Methods

Optical testing. We use a C-band tunable external-cavity diode laser with fibre-coupled output as a light source for testing, which is passed through a fibre isolator and then to a set of fibre polarization controllers. A 90% fused fibre coupler is added between the laser and the polarization controller to tap the laser light for a Mach–Zehnder interferometer and a wavelength meter (wavemeter, 40 MHz resolution) for frequency measurements. We use the wavemeter to precisely measure modes frequencies within the external-cavity diode laser tuning range, to characterize the dispersion of PhCRs. For comb generation experiments, the laser is amplified using an erbium-doped fibre amplifier (EDFA), with a tunable band-pass filter to suppress the amplified spontaneous emission of the EDFA. For passive measurements, the EDFA and the filter are bypassed. We send the light into the photonic chip using a lens fibre mounted on a three-axis flexure stage, controlled by manual micrometers. The damage threshold of our devices is typically above 1 W incident power. The typical coupling efficiency between fibre and chip is ~25% per facet, limited by the mode mismatch between the air-clad waveguides and lens fibres. The chip is placed on a copper block for thermal contact. The output is collected with another lens fibre on translation stage. For passive measurements, we measure the outcoming power using an amplified photodetector, plotting the transmission versus frequency on an oscilloscope.

During the comb generation experiments, we continuously monitor a portion of the outcoupled light with an optical spectrum analyser (OSA). With photodetectors that have 150 MHz bandwidth, we also monitor the pump laser transmission of the resonator and the comb power, which we obtain by filter out the pump contribution. The comb power signal provides critical information on break-up of the flat background and soliton initiation, and for monitoring the intensity noise level of soliton states. To diagnose breather soliton oscillations and perform intensity noise measurements, we use a high-speed photodetector (1.6 GHz bandwidth) and a electronic spectrum analyser.

The comb power channel, after filtering out the pump, is used for the beatnote measurements. We pass the comb light through two cascaded electro-optic phase modulators, driven far above V_π to introduce multiple sidebands to span the 1 THz frequency spacing between the comb lines shown in Fig. 4b. We choose the electro-optic modulation frequency to be 28.000 GHz so the ±17th sidebands from adjacent comb lines will come into close vicinity. To improve the signal to noise ratio for the beatnote measurements, we amplify the electro-optic output with a semiconductor optical amplifier and select the overlapping modes using a tunable optical filter with a 50 GHz passband.

Design and fabrication. We begin the designing process by calculating the ring resonator dispersion and photonic bandgap using a finite-element method programme. All devices in this work are designed and operated using the fundamental transverse electric-like mode. The dispersion calculation yields the propagation constant k_{eff} for each RW, ring radius (R) and frequency. The azimuthal mode order (m) of the PhC is then calculated by the boundary condition $k_{\mathrm{eff}} \times 2\pi R = 2m\pi$. The PhCR modulation is then introduced with the periodicity $2\pi R/2m$ and sinusoidal peak-to-peak amplitude (A_{PhC}) on the interior of the ring. The sinusoidal shape is chosen as it can be fabricated reliably to very small amplitude using lithography and plasma etching. A bus waveguide approaches the smooth outer edge of the resonators. The strength of the evanescent coupling between the resonator and the bus is controlled by the gap between the two. On the edges of the chips where the bus waveguides terminate, the waveguides are inversely tapered to improve mode-matching to lens fibres. We generated the mask files using a pattern-defining script and the CNST Nanolithography Toolbox[40]. Typically, we place up to 70 PhCRs and their bus waveguides per chip in an evenly spaced array. Fine sweeps of A_{PhC} and the coupling gap are included to achieve the correct mode shifts and near-critical coupling[41].

The fabrication procedure of our devices is as follows: we obtain 76.2 mm silicon wafers with 380 μm thickness and 3 μm thermal silicon dioxide on both sides. The tantala device layer is deposited onto the wafer to 570 nm thickness by an external supplier. For lithography, we carry out a double spin-coating of ZEP520A resist to reach a total resist thickness of 1 μm, and then expose the resist by electron-beam lithography operating at 100 kV, with a 4 nm step size and an approximately 30 nm spot size. We attribute the substep size control of modulation amplitudes to averaging effects of the many unit cells around the ring. All device patterns are defined on this electron-beam lithography step. We develop the resist and transfer the pattern using plasma etching with an inductively coupled plasma etching tool, and a $CHF_3 + CF_4 + Ar$ chemistry. The ratio between CHF_3 and CF_4 is varied to achieve vertical sidewall, while the argon gas was found to improve sidewall smoothness. The etch selectivity is sufficient to clear the device layer with the resist thickness used. A dicing pattern is put onto the wafer using ultaviolet lithography and the SPR-220 photoresist. We etch through the bottom thermal oxide layer using a plasma etch with $CHF_3 + O_2$ chemistry. The resist is stripped using solvents, and the ultaviolet lithography step is carried out again for the deep-RIE dicing using the $C_4F_8 + SF_6$ chemistry. We then clean the wafer of the fluoro-polymer deposited during the RIE steps using DuPont EKC265 solvent, followed by a Cyantek Nanostrip soak for final cleaning. The chips are then mechanically removed from the wafer and are ready for testing.

Data availability

The data that support the findings of this study are available from the corresponding author on reasonable request.

Code availability

The simulation codes used in this study are available from the corresponding author on reasonable request.

References

40. Balram, K. C. et al. The nanolithography toolbox. *J. Res. Natl Inst. Stand. Technol.* **121**, 464–475 (2016).
41. Bao, C. & Yang, C. Mode-pulling and phase-matching in broadband Kerr frequency comb generation. *J. Opt. Soc. Am. B* **31**, 3074–3080 (2014).

Acknowledgements

Funding was provided by the DARPA DODOS (all authors), and DRINQS and PIPES programmes (S.-P.Y., D.C.C., H.J., S.B.P.). We acknowledge the Boulder Microfabrication Facility, where the devices were fabricated. We thank T. Briles and J. Chiles for a careful reading of the manuscript. This work is a contribution of the US Government and is not subject to copyright. Mention of specific companies or trade names is for scientific communication only, and does not constitute an endorsement by NIST.

Author contributions

S.-P.Y. contributed in the conception, design and fabrication, and performed the optical measurements and theoretical analysis. D.C.C. developed the simulation software and contributed to the theoretical understanding. H.J. initiated the development of the tantala material platform. G.T.M. provided discussions helpful to the conception. K.S. provided input on theory and fabrication development. S.B.P. contributed to the theoretical understanding and supervised the findings of this work. All authors provided feedback and helped shape the research, analysis and manuscript.

Competing interests

The authors declare no competing interests.

Additional information

Supplementary information The online version contains supplementary material available at https://doi.org/10.1038/s41566-021-00800-3.

Correspondence and requests for materials should be addressed to S.-P.Y.

Peer review information *Nature Photonics* thanks Maxim Shcherbakov, Yun-Feng Xiao and the other, anonymous, reviewer(s) for their contribution to the peer review of this work.